

Article

Effect of Nb–Zr–N Alloying Layer on Surface Mechanical Properties and Biocompatibility of Medical 316L Matrix

Ruian Ni , Hongyan Wu , Zhehang Fan, Yihan Wei, Linshan Yu and Fan Jiang

Institute of Advanced Materials and Flexible Electronics (IAMFE), School of Chemistry and Materials Science, Nanjing University of Information Science and Technology, Nanjing 210044, China

* Correspondence: wuhy2009@nuist.edu.cn; Tel.: +86-138-5140-7280

Abstract: The aim of this study is to further improve the mechanical properties, corrosion resistance, and biocompatibility of the material. We propose a novel method via double-glow plasma alloying–nitriding processing to obtain a Nb–Zr–N alloying layer on medical 316L (316LVM). The surface phase composition and microstructure were observed via X-ray diffraction and scanning electron microscope, respectively. The three-dimensional confocal map of the samples was measured via laser profilometer, the static water contact angle was measured via optical contact angle measuring instrument, and the surface reflectivity was measured via spectrophotometer. Results revealed that the obvious Nb₂N and Zr₃N₄ phase and uniform nanoscale cytosolic organization are obtained at the argon–nitrogen ratio of 1:1 and of gradient distribution of nitride composition forms in the alloying layer. The addition of nitrogen element significantly improved the hardness, friction, and wear properties of the samples. The nano-scale structure of Nb–Zr–N layer plays a better protective role for the substrate with high corrosion resistance, and the corrosion resistance rate is approximately one order of magnitude higher than that of the matrix. In addition, the nontoxic Nb–Zr–N alloying layer exhibits excellent biocompatibility for improving the adsorption, proliferation, and differentiation of cells. Therefore, our work provides a feasible method by which to modify the surface of the Nb–Zr alloying layer via ion nitriding and shows the prospect of its application in medical and biological fields.



Citation: Ni, R.; Wu, H.; Fan, Z.; Wei, Y.; Yu, L.; Jiang, F. Effect of Nb–Zr–N Alloying Layer on Surface Mechanical Properties and Biocompatibility of Medical 316L Matrix. *Coatings* **2023**, *13*, 1346. <https://doi.org/10.3390/coatings13081346>

Academic Editors: Isabelle Jauberteau and Jean Louis Jauberteau

Received: 6 July 2023
Revised: 24 July 2023
Accepted: 27 July 2023
Published: 31 July 2023



Copyright: © 2023 by the authors. Licensee MDPI, Basel, Switzerland. This article is an open access article distributed under the terms and conditions of the Creative Commons Attribution (CC BY) license (<https://creativecommons.org/licenses/by/4.0/>).

Keywords: Nb–Zr–N alloying layer; double glow plasma surface alloying technology; friction performance; corrosion resistance; biocompatibility

1. Introduction

Medical 316L stainless steel (316LSS) has been widely used in the field of biological implant materials for a long time because of its biocompatibility and mechanical properties [1–4]. However, under the harsh environment in human body, long-term contact with tissues and cells often leads to the decline of corrosion resistance and the release of internal elements [5], which seriously affects the service life and may endanger the human body [6]. Moreover, the lower friction performance of bare 316LSS leads to the decrease in mechanical properties during long-term activities [7,8]. Therefore, the surface of matrix must be modified to improve its surface roughness [9], chemical composition [10], wettability [11], corrosion resistance [12], and biocompatibility.

Surface treatment technology is a promising method because of its low cost and simple preparation [13–16]. It has taken a long time to improve medical 316LSS by plasma surface modification to form alloying layer with special structures and properties [17–19]. Niobium (Nb) [20], zirconium (Zr) [21], and other elements [22] with excellent biocompatibility and bone tissue inductivity are widely used to improve the surface properties of bio-implant materials. Some scholars have found that increasing the content of Nb in Nb–Zr alloy will improve the initial mechanical properties [23], corrosion resistance [24], and biocompatibility [25] of the samples, which is beneficial for the application in biomedical

materials. In addition, others have also studied the properties of the materials compounded with Ti-Nb-Zr, showing good corrosion resistance and biocompatibility [26,27], and the increase in Nb content stabilizes the formation of passive film and reduces the sensitivity of pitting corrosion [28]. In our previous research, Nb-Zr alloying layers formed on 316L stainless steel exhibit the great corrosion resistance and biocompatibility. However, due to the poor hardness and wear resistance, Nb-Zr alloys struggle to meet the requirements of long-term activities in the fields of implants [18].

Nitrides often have a special surface structure which can provide an advantageous surface for cell adhesion and growth to solve this problem [29–31]. In recent years, there have been many studies concerning surface coatings used to improve the biocompatibility of materials, such as composite coatings of graphene oxide and copper [32], hydrogel-based coatings [33], soft diamond-like carbon coatings [34], and drug coatings [35]. Moreover, the excellent mechanical properties of nitride coatings attract much attention due to its significant improvement in the hardness and wear resistance of matrix, and it has broad application potential in the field of medical implantation [36–38]. Liu et al. [39] prepared the nitride layer by combining the laser surface texturing and plasma nitriding, which can improve the tribological properties of Zr-2.5Nb alloy. The results showed that plasma nitriding is more advantageous than laser surface texturing, and Zr-2.5Nb alloy fabricated by composite technologies has the highest microhardness and the lowest wear rate. Both Braz et al. [40] and Ezequiel et al. [41] have used plasma nitriding to modify the surface of stainless steel. The former found that during the 24 h incubation period, cell viability on the nitrided surface was higher than that of the polished surface, and the latter analyzed worn surfaces, weight loss curves, and wear debris, which found that the nitriding improved the wear resistance of the tribological system. Furthermore, some scholars also found that magnetron sputtering nitriding on Zr substrate can further improve the original mechanical properties and biocompatibility of Zr-based metals and improve its application in biomedicine by combining its bone-bonding ability [42] and tribological application [43].

The double glow plasma surface alloying (DGPSA) technology in the field of surface treatment is remarkable because its several advantages include free of pollution, gradient distribution of alloying elements, and strong bonding between matrix and alloying layer [44]. The process parameters of the DGPSA ion nitriding process affect the glow-discharge characteristics, and a strong glow-plasma region can be obtained at high air pressure, which provides enough kinetic energy for the ionization and migration of nitrogen atoms. In addition, the control of nitriding layer thickness is also the key to the nitriding process and indicates that the thicker the nitriding layer, the stronger the load-bearing capacity and the better the mechanical properties [45]. The argon to nitrogen ratio in DGPSA ion nitriding process has an important influence on the sputtering amount of nitrogen atoms, as well as the adsorption and diffusion of nitrogen atoms on the surface [46]. Therefore, the selection of a suitable argon-to-nitrogen ratio is essential for the nitriding process. Based on the previous research [18], the nitride on the surfaces of the obtained alloying layers with different argon–nitrogen ratios will obtain better mechanical properties, such as higher hardness and friction resistance, without losing good corrosion resistance and biocompatibility.

In this work, Nb-Zr-N alloying layers were prepared on the surface of 316LVM via the DGPSA technology. The effects of different argon–nitrogen ratios on the surface morphology, microstructure, mechanical properties, friction performance, corrosion resistance and biocompatibility were studied. To further improve the mechanical properties, corrosion resistance and biocompatibility of the 316LVM matrix, the dense, and high hardness alloying layers are prepared through regulating the argon–nitrogen ratio. Simultaneously, a gradient nitride layer was designed by preparing a gradient alloying layer during the double glow plasma nitriding process. Our research will be benefit for obtaining an efficient preparing gradient alloying-nitride layers.

2. Materials and Methods

2.1. Experimental Materials and Structures

To improve the plasma concentration and uniformity, the metal cage hollow-cathode structure formed by the double-layer nested structure is adopted to improve the ionization rate of nitrogen element, shown in Figure 1a,b. The sample is placed inside the double-layer nested structure so that the high concentration of nitrogen plasma will be uniformly covered. When a voltage is applied to the cathode, each hole in the metal mesh will produce a hollow cathode effect. The cross-linked glow plasma will obtain a higher ionization rate, so that the nitrogen in the central part is fully ionized to form a strong plasma of nitrogen and uniformly cover on the sample surface for continuous and stable deposition [47]. In addition, the hollow-cathode structure can also increase the cathode current and the surface temperature of the sample and accelerate the diffusion of nitrogen elements.

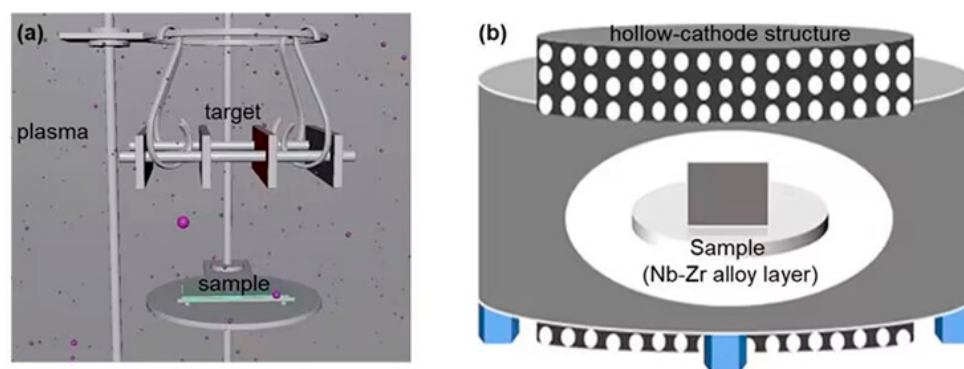


Figure 1. (a) Schematic diagram of plasma surface alloying in the device. (b) Metal cage hollow-cathode structure for Nb–Zr–N alloying layers.

The preparation of Nb–Zr alloying layers on 316LSS by using DGPSA can be referred in the previous research [18]. The 316LVM (20 mm × 20 mm × 3 mm) is chosen as the substrate in this work, and the argon-to-nitrogen ratio is mainly considered as the main processing parameter in this study. During the preparation stage, the Nb–Zr alloyed samples are put into the DGPSA device and pumped the air pressure in the chamber below 6×10^{-4} Pa, then the argon and nitrogen are introduced into the chamber as required proportion according to Table 1. The voltages at both sides were controlled to be 700 V and 400 V, respectively, and different argon–nitrogen ratios of 1:1 (N1), 2:1 (N2), and 2:3 (N3) were selected. We adjusted the gas pressure in the chamber to 90 Pa and controlled the voltage to keep the temperature at 800 °C for 4h-nitriding. The experimental parameters of the ion-nitriding Nb–Zr-based alloying layer are shown in Table 1.

Table 1. Experimental parameters of Nb–Zr-based alloying layers nitrided by DGPSA technique.

Samples	Label	Ar/N Ratio	Working Pressure/Pa	Working Hour/h	Working Temperature/°C
Nitrogen Doped Nb–Zr Alloying layer	N1	1:1	90	4	800
	N2	2:1			
	N3	2:3			

2.2. Phase Analysis and Surface Morphology

X-ray diffractometer (XRD, Smart Lab/3 kW, Rigaku, Tokyo, Japan) was used to analyze the phase composition of the sample surface under different argon–nitrogen ratios. The diffractometer used continuous scanning mode and scanned from 10° to 90° with a scanning speed of 4°/min. Scanning electron microscope (SEM, Gemini 300, Carl Zeiss Meditec AG, Oberkochen, Germany) was used to observe the micro-morphology of the surface and cross sections of the samples prepared under different argon–nitrogen ratios,

and the element distribution and content of the cross section were analyzed with a matching energy dispersive spectroscopy (EDS, Bruker, Billerica, MA, USA).

The three-dimensional morphology of the sample was measured via laser profilometer (SM-1000, Think Focus, Shanghai, China), and its surface roughness was calculated by the following formula:

$$R_q = \sqrt{\frac{1}{n} \sum (Z_i - Z)^2}, \quad (1)$$

where R_q is the root mean square roughness, n is the number of sampling points, Z_i is the height of the i -th sampling point, and Z is the average height of all sampling points.

The static water contact angle of the sample surface was measured by optical contact angle goniometer (JC2000D, Powereach, Shanghai, China), and the diffuse reflectance of the sample surface was obtained via spectroscopy (UV-3600 Plus, Shimadzu, Kyoto-fu, Japan) to reflect the surface structure of the materials.

2.3. Mechanical Property

The friction properties of the samples were tested by a comprehensive tester (CFT-I, Zhongke Kaihua, Changzhou, China), and the method of reciprocating friction in atmospheric environment was adopted. Specifically, the loading load of 0.5 N was selected, the distance and frequency were 5 mm and 2 Hz, respectively, and the testing time was 30 min. Then, the surface topography of the samples after friction was drawn by a three-position topography profiler (Micro XAM 3D, Thinkfocus, Shanghai, China). Moreover, nano-indentation (TI-900, Hysitron, Billerica, MA, USA) was used to test the nano-hardness of the alloying layer by loading-unloading experiment. The diamond indenter was used in the test, which was gradually increased to 3 mN by linear loading. The loading and unloading rates were 6 mN/min, and the maximum indentation depth was 200 nm.

2.4. Electrochemical Measurement

The electrochemical performance of the matrix and Nb–Zr–N alloying layers were tested via electrochemical workstation (CHI660, CH Instruments, Shanghai, China), and the workstation and working schematic diagram are shown in the Figure 2. After packaging and exposing the test area of 1 cm², all the samples were tested at room temperature. First, the samples were put in the 3.5% NaCl solution for 3600 s to test their open circuit voltage, and then the potentiodynamic polarization curve was scanned in the voltage range from –1 to 1 V with the speed of 10 mV/min according to the open circuit voltage.

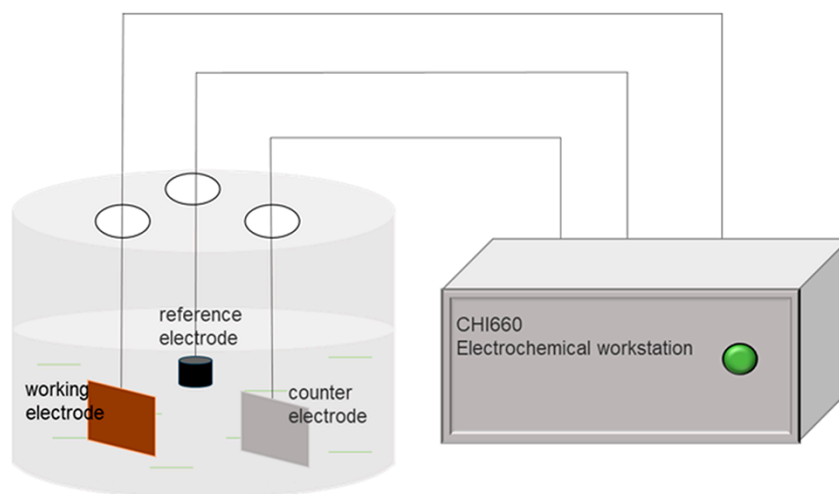


Figure 2. Electrochemical workstation and working schematic diagram.

Similarly, a batch of samples and substrates were packaged and exposed with an area of 1 cm², placed in a beaker filled with Hanks' solution, and kept at 37 °C in a water

bath pot (HH-2, Putian instrument, Changzhou, China) to simulate the corrosion in the body fluid environment. The specific components of Hanks' solution are shown in Table 2. Samples were soaked in water bath at 37 °C for 30 days; then, they were taken out and dried. Finally, the surface corrosion microscopic were tested by SEM.

Table 2. The main component of Hanks' simulated body fluids.

Compositions	NaCl	CaCl ₂	KCl	Na ₂ CO ₃	MgSO ₄ ·7H ₂ O	MgCl·6H ₂ O	Na ₂ HPO ₄ ·2H ₂ O	KH ₂ PO ₄	Glucose
Concentration (g/L)	8.00	0.14	0.40	0.35	0.06	0.10	0.06	0.06	1.00

2.5. Biocompatibility Test

The cytotoxicity on the surface of Nb–Zr–N alloying layer was evaluated via the CCK-8 method in an in vitro cell proliferation experiment. The specific principle is that the CCK-8 kit can stain enzymes in cells in the presence of fluorescent dye, and the absorbance of specific wavelength on the culture plate is measured by enzyme-labeled instrument to reflect the number of cells [48]. Therefore, the number of cells can be judged according to the absorbance value on the cell culture plate, thus indirectly evaluating the cell proliferation, and detailed test parameters can be found in the previously published paper [18].

3. Results and Discussion

3.1. Structure Characterize

Figure 3 shows the surface morphology and real image of the Nb–Zr–N alloying layer. The surface structures of the Nb–Zr-based alloying layers nitrided with different argon-to-nitrogen ratios are compact without any defects, which are closely related to the grain growth orientation and particle sputtering during the ion nitriding process. The surface of the N2 sample is relatively flat, and the argon and nitrogen particles move to the surface of the sample at the same time at high speed under the action of electric field. The surface structure of the sample is changed by the back-sputtering of argon particles during the nucleation of the alloying layer. This indicates that the phenomenon of nitride aggregation occurred during the nitriding process, which is related to the enrichment effect of nitrogen elements. Combined with the distribution of elemental content on the surface of the Nb–Zr–N alloying layer in Table 3, the surface of the 316LVM substrate is composed of four elements—N, Nb, Zr and Fe—indicating that a certain amount of nitrogen has been deposited on the surface of the alloying layer and a nitride phase has been formed.

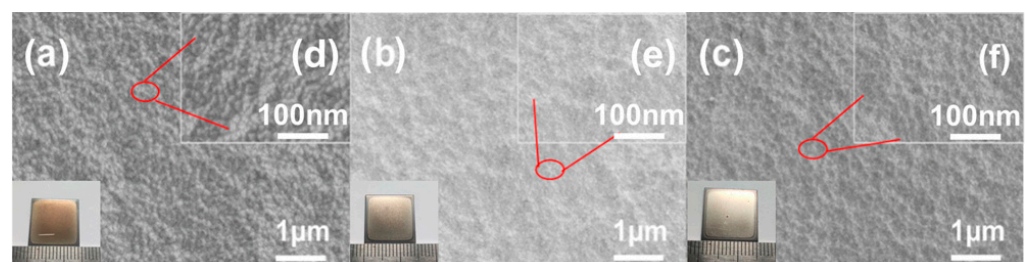


Figure 3. Surface morphologies of Nb–Zr–N alloying layers (a) N1, (b) N2, (c) N3, and their partial enlarged views (d,e,f) are indicated by red highlighted marks, respectively. The real images of the coated parts are in the left corner.

Table 3. Distribution of elemental content on the surface of Nb–Zr–N alloying layers.

Samples	Ar/N ₂ Ratio	N/wt. %	Nb/wt. %	Zr/wt. %	Fe/wt. %
N1	1:1	9.52	87.42	1.13	1.93
N2	2:1	6.05	90.16	1.07	2.72
N3	2:3	12.30	84.87	1.52	1.31

Figure 4 illustrates the cross-sectional morphology and elemental distribution of Nb–Zr–N alloying layers with different argon–nitrogen ratios. As observed from the figures, the thicknesses of the nitride layers vary, measuring approximately 2.2, 1.4, and 2 μm , respectively. The N1 sample exhibits the thickest nitride layer, while the nitride layers in the other samples are thinner. It is evident that as the nitrogen content decreases and the argon content increases, more vacancies and energy are generated upon impact with the surface. However, this also leads to an increase in the back sputtering of various elements on the surface, ultimately resulting in a thinner nitride layer. Moreover, excessively high nitrogen content leads to a relative reduction in argon ions, causing the energy of nitrogen deposited on the substrate surface to be too low for diffusion. Consequently, this can lead to the formation of a thinner nitride layer.

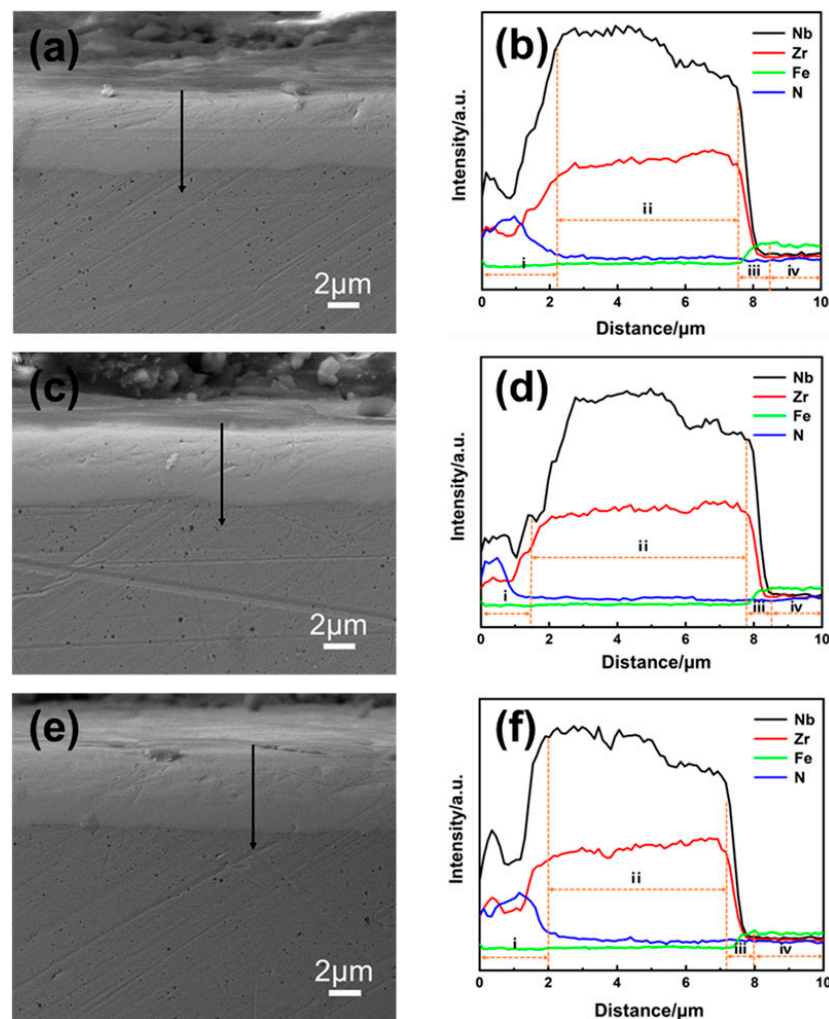


Figure 4. Cross-sectional morphology of Nb–Zr–N alloying layer: (a) N1, (b) N2, (c) N3 and their corresponding elemental distribution: (d–f), and different compositions of the sample varying with depth: (i) nitride layer; (ii) deposition layer; (iii) diffusion layer; (iv) substrate.

Figure 5 displays the XRD patterns of the Nb–Zr–N alloying layers. From this figure, a certain amount of nitride was generated on the surface of the sample after DGPSA ion nitriding, and the diffraction peaks show the presence of Nb, Zr, Nb_2N (JCPDS#40-1274), Zr_3N_4 (JCPDS#51-0646), and $\text{FeN}_{0.0324}$ phases. The surface of the N1 sample exhibits the diffraction peaks of Nb_2N , Zr_3N_4 , and $\text{FeN}_{0.0324}$. Nb_2N and Zr_3N_4 phases are grown along the (101) and (131) crystal planes at the 2-Theta angle of 38.5° in a selective orientation, respectively, while the $\text{FeN}_{0.0324}$ phase appears at the 2-Theta angles of 43.9° , 50.8° , and 74.6° . This can be explained by the ion bombardment effect, which leads to densification

and orientation of the Nb_2N and Zr_3N_4 phases. A suitable argon-to-nitrogen ratio induces enhanced mobility of nitrogen, making the grains crystallize more easily at low surface energy. The characteristic peaks of Nb and Zr phases on the surface of the N2 sample are still sharp and strong, and the peaks of Nb_2N , Zr_3N_4 , and $\text{FeN}_{0.0324}$ phases are all smaller, indicating that the nitrogen content decreases, and the generation of the nitride phases is hindered. The nitride phases on the surface of the N3 sample are more complex, with the appearance of Nb and Zr in the second phase. The atomic clusters are easily formed in the enriched nitride environment, leading to the orientation transition of Nb and Zr, and the Nb_2N and Zr_3N_4 phases generated on the surface of the Nb–Zr-based alloying layer are differently oriented, causing a change in the surface structure of the alloying layer. The Nb–Zr-based alloying layer with a selectively oriented nitride layer provides a theoretical basis for the improvement of surface hardness, wear resistance, and biocompatibility.

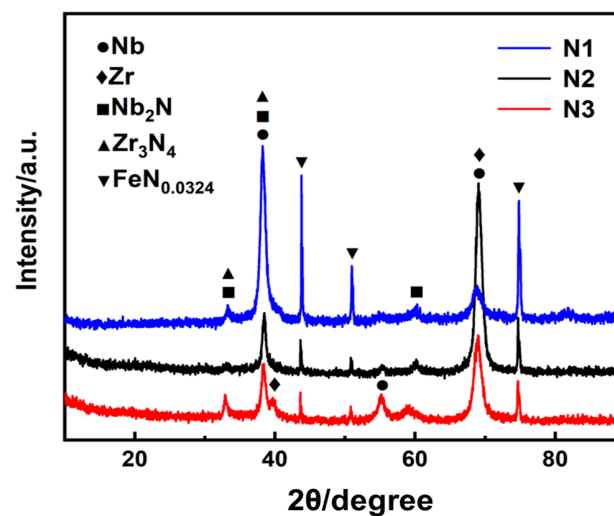


Figure 5. XRD patterns of Nb–Zr–N alloying layers.

3.2. Research of Surface State

Figure 6 manifests the three-dimensional confocal map of the surface of the Nb–Zr–N alloying layer and virgin sample with Nb–Zr surface without nitriding. The surface roughness of the nitride layer varies with the grain size, growth orientation, and the sputtering of the particles. The surface of the N1 sample shows a compact cellular structure with uniform size of the nanostructure and a surface roughness R_q of 0.65 μm . The surface of the N2 sample displays a gentler surface structure, which is related to the appropriate argon–nitrogen ion sputtering, with a surface roughness R_q of 0.61 μm . The N3 sample reveals an aggregated raised structure with large undulations and a maximum surface roughness R_q of 0.96 μm . The sample with the Nb–Zr surface without nitriding shows a surface roughness R_q of 0.62 μm , which is close to the N1 and N2 sample but much less than N3 sample.

Figure 7 shows the surface water contact angle and UV reflectance values of the Nb–Zr–N alloying layer, which is useful to reflect the surface roughness variation. The surface water contact angles of N1, N2, and N3 samples are 120°, 96° and 106°, respectively, indicate that they have certain abilities of hydrophobicity compared to 316LVM substrate (67°). The ultraviolet reflectance of the N2 sample is obviously lower than that of N1 and N3, which also corresponds to the smallest contact angle of surface water and close to 316LVM when the wavelength is high. However, the largest surface roughness of the N3 sample fails to form a homogeneous nanoscale cellular structure, so the surface water contact angle values are smaller than those of N1.

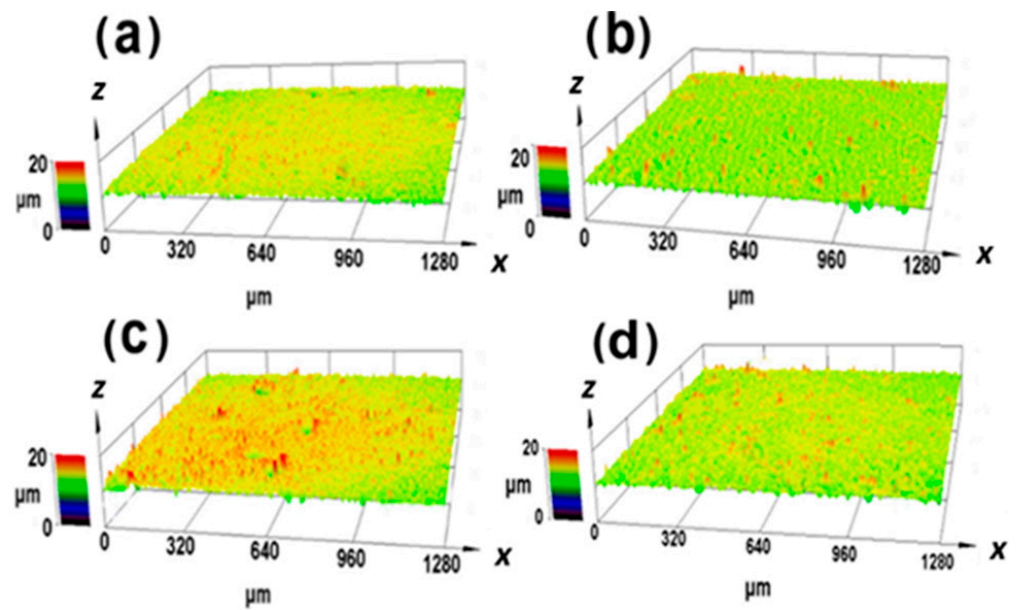


Figure 6. Three-dimensional confocal map of Nb–Zr–N alloying layer surface: (a) N1, (b) N2, (c) N3, and (d) virgin sample with Nb–Zr surface.

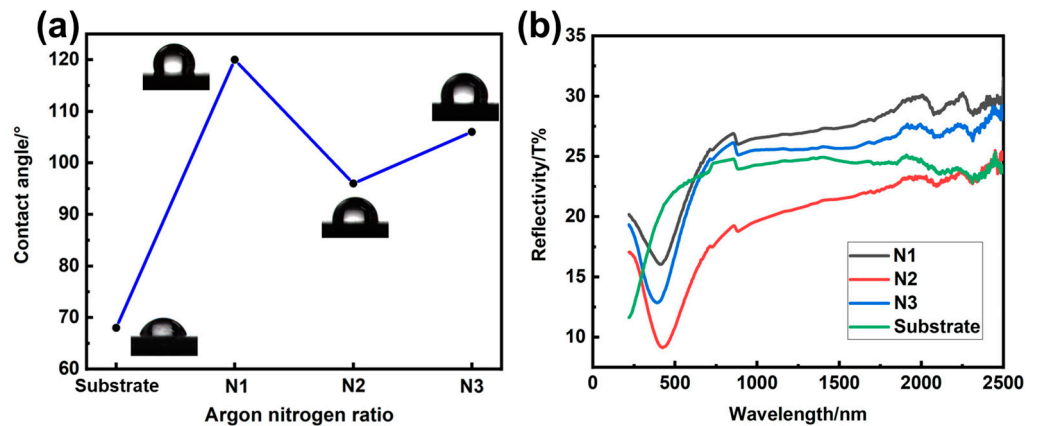


Figure 7. (a) The water contact angle and (b) UV reflection diagram of Nb–Zr–N alloying layer surface.

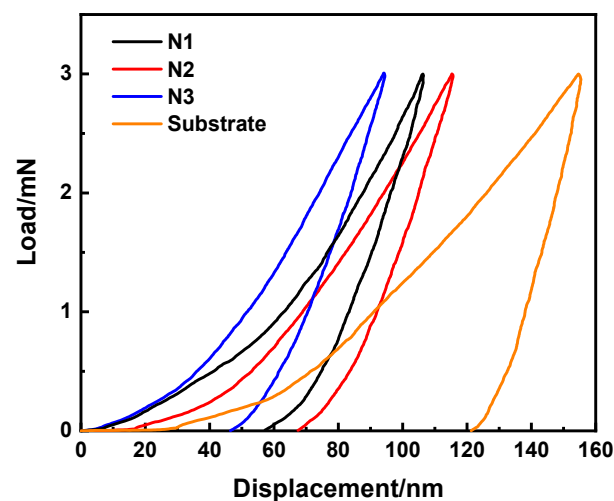
3.3. Research of Mechanical Performance

Surface hardness is one of the important mechanical properties of the alloying layer, which largely affects the level of wear resistance. Increasing hardness generally reduces the friction coefficient and improves the wear resistance of the alloying layer. The Nb–Zr–N alloying layer generates a hard nitride phase, and the surface hardness is already much greater than that of bare medical 316LVM. As shown in Table 4, the surface hardness of N1, N2, and N3 samples were 20.54, 18.83, and 22.79 GPa, respectively, which is harder than the matrix. The increase in the surface hardness of the alloying layer is related to the formation of the nitride phase, and both Nb_2N and Zr_3N_4 have high hardness and strong chemical stability [49]. What is more, the effect of grain size on the hardness of crystal materials can be explained by Hall–Petch relationship [50] combined with a transition from dislocation-based plasticity to grain boundary sliding, rotation, or diffusion as the main mechanism responsible for hardness [51].

Table 4. Surface hardness data of Nb–Zr–N alloying layers.

Samples	Hardness H/GPa
316LVM	5.16
With Nb–Zr Surface	8.02
N1	20.54
N2	16.83
N3	22.79

Figure 8 shows the variation of the surface load with the displacement of the Nb–Zr–N alloying layer. At the same loading load, the alloys' indentation depths corresponding to different argon–nitrogen ratios are different. The load–displacement curve changes continuously throughout the loading and unloading process, and there is a great rebound after unloading, indicating that the alloying layers exhibit excellent toughness. The N1 sample has a high surface hardness, and the indentation depth is about 106 nm when the maximum load is 3 mN. This can be interpreted as the surface of the alloying layer has a certain preferred orientation, leading to a strong grain boundary consistency, and the grain boundary slip is difficult, so the surface plastic deformation resistance is enhanced. The surface of the N2 sample has a low degree of nitridation, and the depth of indentation can reach 115 nm. The indentation depth of the N3 sample is 94 nm only, and the surface hardness is the largest, which makes the alloying layer springs back quickly after loading and unloading. It is related to the complex covalent bond structure of the nitrided phase on the surface of the alloying layer, and the covalent bond is directional, which can improve the creep resistance of the surface.

**Figure 8.** Variation of surface load with displacement of Nb–Zr–N alloying layer.

3.4. Research of Friction Properties

Figures 9 and 10 display the surface wear-track morphologies of the medical 316LVM and Nb–Zr–N alloying layers. The width and depth of the wear trace along the friction direction on the surface of 316LVM are relatively large and the surface shows obvious scratches and furrows, which indicate low wear resistance. In the grinding process of medical 316LVM, due to the low surface hardness, the grinding material is pressed into a larger depth and the contact area is larger, which makes it easier to produce abrasive particles. With the accumulation of abrasive particles, there will be a strong cutting effect on the surface of the substrate, resulting in the gradual deepening and widening of the surface wear trace, which exhibits serious abrasive wear phenomenon during the friction process. The surface wear trace on the Nb–Zr–N alloying layers become significantly shallower, and most of the area is not severely damaged due to the nitride layer. N2 sample has a relatively flat surface structure and a relatively thin surface nitride layer, so the actual

contact area between the surface and the abrasives is larger, and it is easier to rub and tear, resulting in a greater degree of wear. The whole test process of N1 and N3 samples is mainly based on sliding friction with slight abrasive wear because of numerous high hardness nitrides on their surfaces, and they have high surface bearing capacity, causing low abrasive penetration depth and less abrasive particles produced during friction. The N1 sample has lowest wear degree since the uniform nano-scale cellular structure struggles to produce adhesive nodes, which reduces the contact area between the alloying layer and wear-resistant materials, resulting in a significant improvement in wear resistance. Moreover, the wear situation of N1 sample shows large-area sliding wear [52], which decreases the width and depth of wear marks, eventually leading to low wear and slight wear marks.

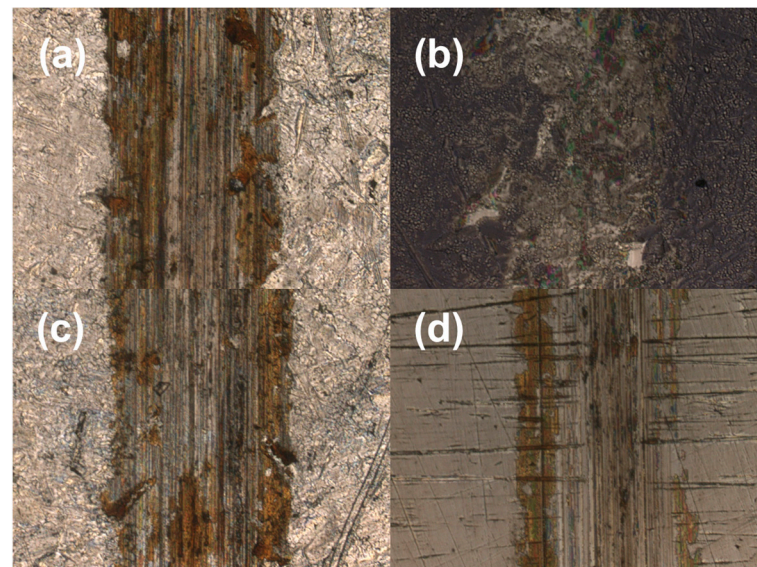


Figure 9. Two-dimensional morphology of (a) 316LVM substrate and (b) N1, (c) N2, and (d) N3 samples with surface wear.

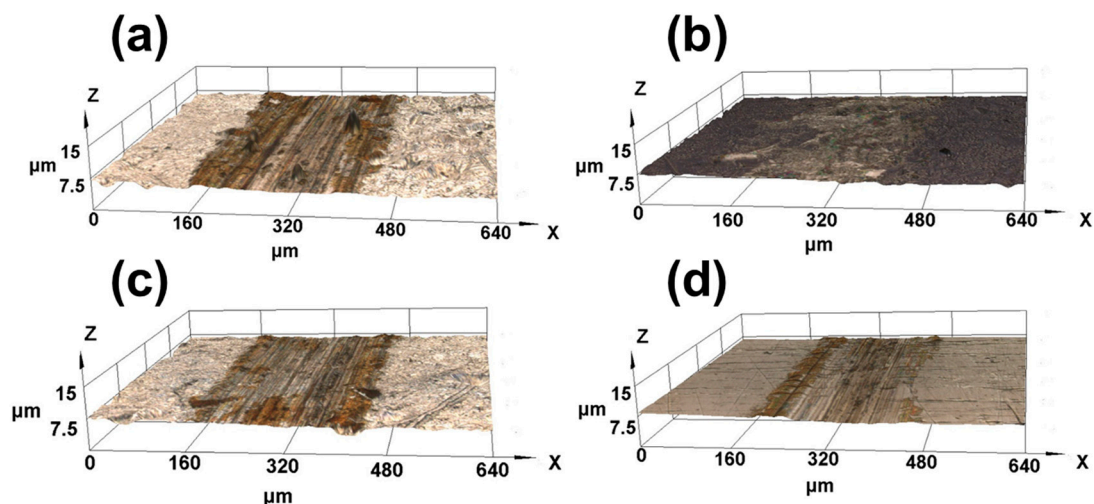


Figure 10. 3D morphology of the surface wear trace (a) 316LVM substrate and (b) N1, (c) N2, and (d) N3 samples.

Figure 11 exhibits the surface wear profile of medical 316LVM and the Nb–Zr–N alloying layer. As shown in Table 5, the width and depth of the wear track on the surface of medical 316LVM are larger, with a specific wear rate K of $600 \times 10^{-6} \text{ mm}^3 \text{ N}^{-1} \text{ m}^{-1}$. When the vertical normal force is applied to the substrate surface, the surface is squeezed,

resulting in increased plastic deformation, and the abrasive wear effect is severe after relative movement occurs, which increases the wear degree. The higher surface hardness of the Nb–Zr–N alloying layers reduce the wear level with specific wear rates K of $30 \times 10^{-6} \text{ mm}^3 \text{ N}^{-1} \text{ m}^{-1}$, $249 \times 10^{-6} \text{ mm}^3 \text{ N}^{-1} \text{ m}^{-1}$, and $160 \times 10^{-6} \text{ mm}^3 \text{ N}^{-1} \text{ m}^{-1}$, respectively, and the specific wear rates K of the Nb–Zr–N alloying layers are 5%, 41.5%, and 26.7% of the substrate, indicating that the nitride layers protect the matrix and improve the wear resistance to some extent. Since the hard nitride layer on the surface of N1 sample has obvious wear-resistant effect, the main sliding friction leads to lower specific wear rate K and the best wear resistance. Otherwise, the surface of N1 sample's uniform nano-scale structure and selectively orientation lead to high roughness, which can reduce the contact area of the abrasive particles and the cutting effect of abrasive particles during friction, resulting in friction performance improved [53].

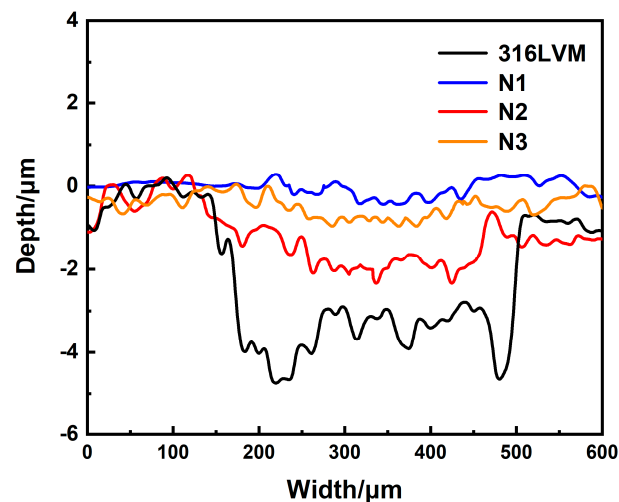


Figure 11. Medical 316LVM and Nb–Zr–N alloying layer surface wear contour diagram.

Table 5. Medical 316LVM and Nb–Zr–N alloying layer surface wear data.

Samples	Wear Depth $h/10^{-3} \text{ mm}$	Wear Width b/mm	Wear Volume $V/10^{-5} \text{ mm}^3$	Wear Ratio $K/10^{-6} \text{ mm}^3 \text{ N}^{-1} \text{ m}^{-1}$
316LVM	4.5	0.36	540	600
N1	0.4	0.20	27	30
N2	2.1	0.32	224	249
N3	1.8	0.24	144	160

3.5. Research of Anti-Corrosion Performance

3.5.1. Dynamic Corrosion Analysis

Figure 12 displays the dynamic potential polarization test curve of Nb–Zr–N alloying layers in 3.5% NaCl solution. In combination with Table 6, the self-corrosion potentials of N1, N2, and N3 samples are obviously shifted positively, which are -0.20 , -0.27 , and -0.22 V, respectively. The N1 sample has a lower corrosion rate, showing better chemical stability and corrosion resistance due to the special structure of nano-nitride. In addition, the alloying layer will form a dense passivation layer with Nb and Zr elements in the solution, which prevents the further corrosion of the internal metal and improves the corrosion resistance. The corrosion current densities of N1, N2, and N3 samples are $7.1 \times 10^{-8} \text{ A cm}^{-2}$, $6.46 \times 10^{-7} \text{ A cm}^{-2}$, and $6.87 \times 10^{-7} \text{ A cm}^{-2}$, respectively, which is significantly reduced compared with the bare medical 316LVM and indicates the better protection of the substrate. The corrosion resistance of the alloying layer depends on the surface structure, and the higher the surface hydrophobicity, the better the corrosion resistance [54].

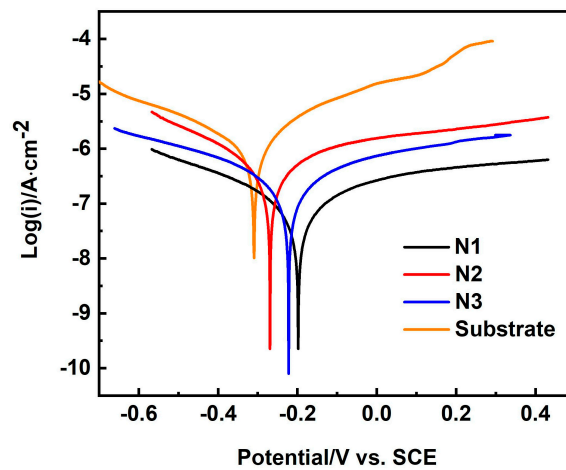


Figure 12. Dynamic potential polarization curve of Nb–Zr–N alloying layer in 3.5% NaCl solution.

Table 6. Corrosion potential, corrosion current, and corrosion rate of Nb–Zr–N alloying layer in 3.5% NaCl solution.

Sample	Corrosion Current $I_{corr}/A\ cm^{-2}$	Corrosion Voltage E_{corr}/V	Corrosion Rate (mm/Year)
316LVM	6.03×10^{-6}	-3.09×10^{-1}	7×10^{-2}
N1	7.10×10^{-8}	-1.98×10^{-1}	8.4×10^{-4}
N2	6.46×10^{-7}	-2.69×10^{-1}	7.6×10^{-3}
N3	6.87×10^{-7}	-2.22×10^{-1}	8.1×10^{-3}

3.5.2. Static Corrosion Analysis

Figure 13 exhibits the surface morphologies of the Nb–Zr–N alloy samples after 30 days of immersion corrosion in Hanks’ solution. After the immersion corrosion at 37 °C for 30 days, N1 sample’s surface integrity is preserved, which is still uniform and has dense cell structures with only small parts of the dark spots. This is due to the uniform nano-scale cellular structure and excellent hydrophobic property on the surface of N1 sample, which makes corrosive ions not easily adsorbed on the surface and has the best corrosion resistance. Compared with the N1 sample, N2 and N3 samples have different degrees of corrosion. Among them, the N2 sample is seriously corroded with a large number of corrosion pits, while the N3 sample’s surface structures remain relatively intact, and a small number of cellular structures are flattened due to corrosion, resulting in partial corrosion discoloration. The more serious corrosion phenomenon is related to the loss of integrity and compactness of the passivation films, and the decrease in the resistance to corrosive ions leads to the discoloration and roughness increase in the surfaces. Although there are partial corrosion areas after immersion corrosion, the surfaces are still integrated compared with the substrate, which is due to the change of surface microstructure after nitriding [55].

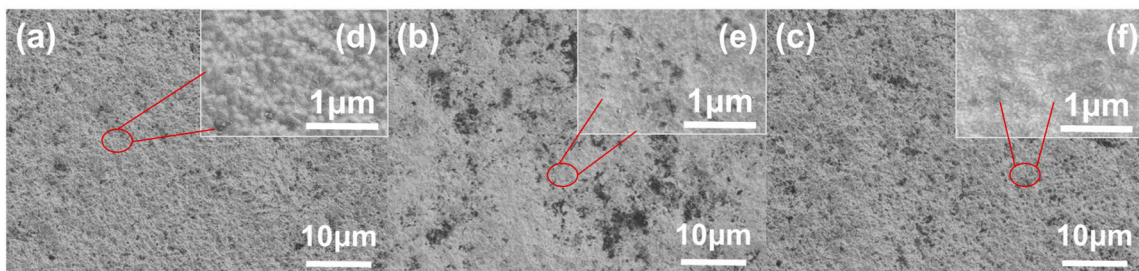


Figure 13. SEM images of Nb–Zr–N alloy samples (a) N1, (b) N2, and (c) N3 immersed in Hanks’ solution at 37 °C for 30 days and their corresponding partial enlarged views (d–f) are indicated by red highlighted marks.

3.6. Research of Biocompatibility

3.6.1. Cell Activity Analysis

Figure 14 presents the cell absorbance data of the blank control, N1, N2, and N3 groups. After the first day, the cell proliferations on these samples were almost similar. When the incubation time reached 3 days, the cell activity on the surface of the alloy samples was obviously much higher, and the cell activity on the surface of N1 group was slightly higher than that of the blank control group and significantly better than that of N2 and N3 groups. After 7 days, the cell absorbance on the surface of N1 group was the highest and still maintained a higher cell activity than the blank control group, and the cell survival rate could reach 110% compared to the blank group. While the cell survival rate of N2 and N3 groups decreased relative to the blank control group, the cell survival rate still maintained a high level [56]. The value of cell activity on the sample surface is related to the biotoxicity of the material surface and the adsorption and proliferation of cells. Medical metal materials inevitably cause the problem of metal ion release, which can lead to a series of issues such as elevated solution pH and changes in environmental osmotic pressure. The Nb–Zr–N alloying layer has excellent surface properties, and its surface is highly resistant to ion invasion during cell proliferation, which does not produce excessive corrosion products or changes the cell culture solution environment.

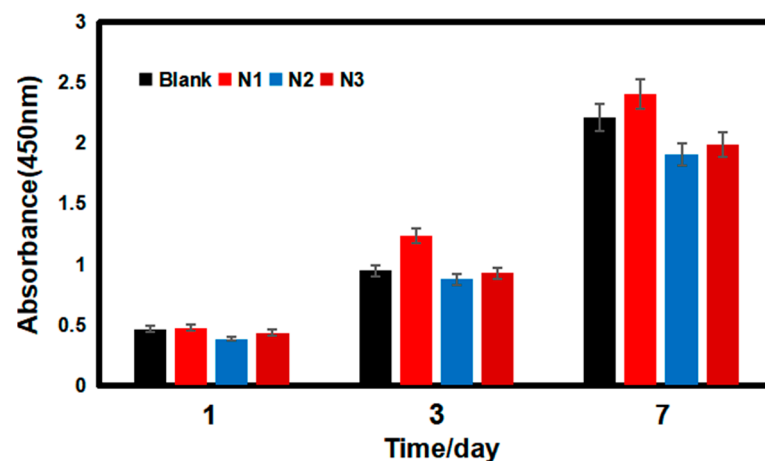


Figure 14. Cell absorbance data of blank control group, N1 group, N2 group and N3 group.

3.6.2. Cell Morphology Studies

Figure 15 reveals the fluorescence confocal plots of cells on the surface of blank control group and Nb–Zr–N alloy samples after 7 days of cell proliferation. The cells grew well on the surface of the Nb–Zr–N alloy samples with dense growth numbers, spreading over the entire surface in a fibrous shape. The relatively high number of cell proliferation on the surface of N1 sample was attributed to the homogeneous nano-cellular structure that could increase the specific surface area of cell–surface contact, which provided active sites for cells and facilitate cell adhesion and growth on the surface [57]. The lowest cell density on the surface of the N2 sample was due to the partial dissolution of the alloying layer, which changed the microenvironment of the culture medium and inhibited cell proliferation. Therefore, the Nb–Zr–N alloying layers can promote cell proliferation to some extent without significant cytotoxicity and has good biocompatibility.

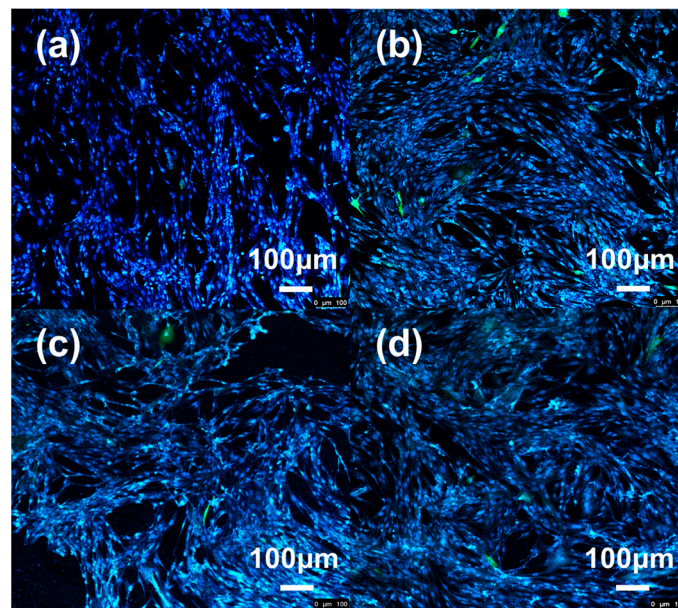


Figure 15. Fluorescence confocal plots after 7 days of cell culture: (a) blank control group, (b) N1 group, (c) N2 group, and (d) N3 group.

4. Conclusions

In this work, Nb–Zr–N alloying layers were prepared on the surface of medical 316LVM using DGPSA technology, and the relationships between the surface morphology, tissue structure, mechanical properties, corrosion resistance, and biocompatibility of Nb–Zr–N alloying layers and the argon-to-nitrogen ratio were investigated, and the following conclusions were obtained:

- (1) The argon-to-nitrogen ratio in the ion nitriding process affects the surface structure and properties of the alloying layers, among which the N1 sample shows uniform nanoscale cytosolic structure with spheres of 100 nm in diameter with 1:1 argon-to-nitrogen ratio;
- (2) The surface hardness of the Nb–Zr–N alloying layer is significantly increased, and the frictional properties are enhanced due to the Nb₂N and Zr₃N₄ formed on the surface of alloying layers with the combination of nanostructures;
- (3) The corrosion resistance of Nb–Zr–N alloying layer is significantly higher than that of medical 316LVM, and the passivation film formed by the oxidation of Nb and Zr can hinder the ion invasion, which plays a better protective role in the substrate;
- (4) The Nb–Zr–N alloying layer promotes the adsorption, proliferation, and differentiation of cells to a certain extent and has no biological toxicity compared with the blank control group, and its good biocompatibility is of great potential as a medical implant material.

Author Contributions: Conceptualization, funding acquisition, writing—review and editing, resources, H.W.; writing—original draft preparation and validation, R.N.; investigation, Z.F., Y.W. and L.Y.; project administration and supervision, F.J. All authors have read and agreed to the published version of the manuscript.

Funding: This project is supported by the Six Talent Peaks Project of Jiangsu Province, China (No. GDZB-046).

Institutional Review Board Statement: Not applicable.

Informed Consent Statement: Not applicable.

Data Availability Statement: The data presented in this study are also available upon request from the corresponding author.

Conflicts of Interest: The authors declare no conflict of interest.

References

1. Liu, X.R.; Liu, W.C.; Wang, H.Y.; Li, V.L.; Chen, Y.H.; Wang, A.N.; Wu, C.J.; Li, Y.Q.; Zhao, G.; Lin, C.P.; et al. Polyelectrolyte multilayer composite coating on 316L stainless steel for controlled release of dual growth factors accelerating restoration of bone defects. *Mat. Sci. Eng. C-Mater.* **2021**, *126*, 112187. [[CrossRef](#)]
2. Hosseini, M.R.; Ahangari, M.; Johar, M.H.; Allahkaram, S.R. Optimization of nano HA-SiC coating on AISI 316L medical grade stainless steel via electrophoretic deposition. *Mater. Lett.* **2021**, *285*, 129097. [[CrossRef](#)]
3. Aqib, R.; Kiani, S.; Bano, S.; Wadood, A.; Ur Rehman, M.A. Ag-Sr doped mesoporous bioactive glass nanoparticles loaded chitosan/gelatin coating for orthopedic implants. *Int. J. Appl. Ceram. Technol.* **2021**, *18*, 544–562. [[CrossRef](#)]
4. Wang, N.; Meenashisundaram, G.K.; Chang, S.; Fuh, J.Y.H.; Dheen, T.; Kumar, A.S. A comparative investigation on the mechanical properties and cytotoxicity of Cubic, Octet, and TPMS gyroid structures fabricated by selective laser melting of stainless steel 316L. *J. Mech. Behav. Biomed.* **2022**, *129*, 105151. [[CrossRef](#)] [[PubMed](#)]
5. Ahmadi, R.; Afshar, A. In vitro study: Bond strength, electrochemical and biocompatibility evaluations of TiO₂/Al₂O₃ reinforced hydroxyapatite sol-gel coatings on 316L SS. *Surf. Coat. Technol.* **2021**, *405*, 126594. [[CrossRef](#)]
6. Kedia, S.; Bonagani, S.K.; Majumdar, A.G.; Kain, V.; Subramanian, M.; Maiti, N.; Nilaya, J.P. Nanosecond laser surface texturing of type 316L stainless steel for contact guidance of bone cells and superior corrosion resistance. *Colloid Interface Sci.* **2021**, *42*, 100419. [[CrossRef](#)]
7. Li, H.F.; Huang, J.Y.; Lin, G.C.; Wang, P.Y. Recent advances in tribological and wear properties of biomedical metallic materials. *Rare Met.* **2021**, *40*, 3091–3106. [[CrossRef](#)]
8. Moghadasi, K.; Isa, M.S.M.; Ariffin, M.A.; Jamil, M.Z.M.; Raja, S.; Wu, B.; Yamani, M.; Bin Muhamad, M.R.; Yusof, F.; Jamaludin, M.F.; et al. A review on biomedical implant materials and the effect of friction stir based techniques on their mechanical and tribological properties. *J. Mater. Res. Technol.* **2022**, *17*, 1054–1121. [[CrossRef](#)]
9. Karthikeyan, S.; Mohan, B.; Kathiresan, S.; Anbuhezhiyan, G. Effect of process parameters on machinability, hemocompatibility and surface integrity of SS 316L using R-MRAFF. *J. Mater. Res. Technol.* **2021**, *15*, 2658–2672. [[CrossRef](#)]
10. Gawad, S.A.; Nasr, A.; Fekry, A.M.; Filippov, L.O. Electrochemical and hydrogen evolution behaviour of a novel nano-cobalt/nano-chitosan composite coating on a surgical 316L stainless steel alloy as an implant. *Int. J. Hydrogen Energy* **2021**, *46*, 18233–18241. [[CrossRef](#)]
11. Parau, A.C.; Juravlea, G.A.; Raczkowska, J.; Vitelaru, C.; Dinu, M.; Awsuiuk, K.; Vranceanu, D.M.; Ungureanu, E.; Cotrut, C.M.; Vladescu, A. Comparison of 316L and Ti6Al4V biomaterial coated by ZrCu-based thin films metallic glasses: Structure, morphology, wettability, protein adsorption, corrosion resistance, biomineralization. *Appl. Surf. Sci.* **2023**, *612*, 155800. [[CrossRef](#)]
12. Zhang, S.; Liang, X.J.; Gadd, G.M.; Zhao, Q. A sol-gel based silver nanoparticle/polytetrafluoroethylene (AgNP/PTFE) coating with enhanced antibacterial and anti-corrosive properties. *Appl. Surf. Sci.* **2021**, *535*, 147675. [[CrossRef](#)]
13. Kaliaraj, G.S.; Siva, T.; Ramadoss, A. Surface functionalized bioceramics coated on metallic implants for biomedical and anticorrosion performance—A review. *J. Mater. Chem. B* **2021**, *9*, 9433–9460. [[CrossRef](#)]
14. Liao, T.Y.; Biesiekierski, A.; Berndt, C.C.; King, P.C.; Ivanova, E.P.; Thissen, H.; Kingshott, P. Multifunctional cold spray coatings for biological and biomedical applications: A review. *Prog. Surf. Sci.* **2022**, *97*, 100654. [[CrossRef](#)]
15. Shah, R.; Gashi, B.; Hoque, S.; Marian, M.; Rosenkranz, A. Enhancing mechanical and biomedical properties of prostheses—Surface and material design. *Surf. Interfaces* **2021**, *27*, 101498. [[CrossRef](#)]
16. Hernandez Navarro, C.; Flores Martinez, M.; Camps Carvajal, E.E.; Rivera Resendiz, L.P.; Garcia Bustos, E.D. Analysis of the wear behavior of multilayer coatings of TaZrN/TaZr produced by magnetron sputtering on AISI-316L stainless steel. *Int. J. Adv. Manuf. Technol.* **2021**, *117*, 1565–1573. [[CrossRef](#)]
17. Resnik, M.; Bencina, M.; Levicnik, E.; Rawat, N.; Igljic, A.; Junkar, I. Strategies for improving antimicrobial properties of stainless steel. *Materials* **2020**, *13*, 2944. [[CrossRef](#)]
18. Zhao, K.; Wu, H.Y.; Xiao, C.L.; Dong, J.; Ren, J.; Peng, Z. Study on corrosion resistance and biological properties of the double glow plasma Nb-Zr biological implantation alloying layers. *Coatings* **2022**, *12*, 942. [[CrossRef](#)]
19. Tekdir, H.; Yetim, T.; Yetim, A.F. Corrosion properties of ceramic-based TiO₂ films on plasma oxidized Ti6Al4V/316L layered implant structured manufactured by selective laser melting. *J. Bionic. Eng.* **2021**, *18*, 944–957. [[CrossRef](#)]
20. Chandra, G.; Pandey, A. Design approaches and challenges for biodegradable bone implants: A review. *Expert Rev. Med. Devices* **2021**, *18*, 629–647. [[CrossRef](#)]
21. Anju, S.; Mohanan, P.V. Biomedical applications of transition metal dichalcogenides (TMDCs). *Synth. Met.* **2021**, *271*, 116610. [[CrossRef](#)]
22. Fattah-alhosseini, A.; Chaharmahali, R.; Keshavarz, M.K.; Babaei, K. Surface characterization of bioceramic coatings on Zr and its alloys using plasma electrolytic oxidation (PEO): A review. *Surf. Interfaces* **2021**, *25*, 101283. [[CrossRef](#)]
23. Akahori, T.; Niinomi, M.; Nakai, M.; Tsutsumi, H.; Kondo, Y.; Hattori, T.; Fukui, H. Mechanical properties and biocompatibilities of Zr-Nb system alloys with different Nb contents for biomedical applications. *J. Jpn. Inst. Met.* **2011**, *75*, 445–451. [[CrossRef](#)]
24. Zhou, F.Y.; Wang, B.L.; Qiu, K.J.; Lin, W.J.; Li, L.; Wang, Y.B.; Nie, F.L.; Zheng, Y.F. Microstructure, corrosion behavior and cytotoxicity of Zr-Nb alloys for biomedical application. *Mat. Sci. Eng. C-Mater.* **2012**, *32*, 851–857. [[CrossRef](#)]

25. Lou, B.S.; Lin, T.Y.; Chen, W.T.; Lee, J.W. Corrosion property and biocompatibility evaluation of Fe-Zr-Nb thin film metallic glasses. *Thin Solid Films* **2019**, *691*, 137615. [[CrossRef](#)]
26. Gulsoy, H.O.; Pazarlioglu, S.; Gulsoy, N.; Gundede, B.; Mutlu, O. Effect of Zr, Nb and Ti addition on injection molded 316L stainless steel for bio-applications: Mechanical, electrochemical and biocompatibility properties. *J. Mech. Behav. Biomed.* **2015**, *51*, 215–224. [[CrossRef](#)]
27. Zhang, T.; Ou, P.; Ruan, J.; Yang, H. Nb-Ti-Zr alloys for orthopedic implants. *J. Biomater. Appl.* **2021**, *35*, 1284–1293. [[CrossRef](#)]
28. Ji, P.F.; Li, B.; Chen, B.H.; Wang, F.; Ma, W.; Zhang, X.Y.; Ma, M.Z.; Liu, R.P. Effect of Nb addition on the stability and biological corrosion resistance of Ti-Zr alloy passivation films. *Corros. Sci.* **2020**, *170*, 108696. [[CrossRef](#)]
29. Li, L.; Yao, S.L.; Zhao, X.L.; Yang, J.J.; Wang, Y.X.; Wang, L.N. Fabrication and properties of anodic oxide nanotubular arrays on Zr-17Nb alloy. *Acta Metall. Sin.* **2019**, *55*, 1008–1018. [[CrossRef](#)]
30. Fontoura, C.P.; Bertele, P.L.; Rodrigues, M.M.; Dotta Maddalozzo, A.E.; Frassini, R.; Celi Garcia, C.S.; Martins, S.T.; Crespo, J.d.S.; Figueroa, C.A.; Roesch-Ely, M.; et al. Comparative Study of Physicochemical Properties and Biocompatibility (L929 and MG63 Cells) of TiN Coatings Obtained by Plasma Nitriding and Thin Film Deposition. *ACS Biomater. Sci. Eng.* **2021**, *7*, 3683–3695. [[CrossRef](#)] [[PubMed](#)]
31. Moura, C.E.B.; Queiroz Neto, M.F.; Braz, J.K.F.S.; Aires, M.d.M.; Silva Farias, N.B.; Barboza, C.A.G.; Cavalcanti Junior, G.B.; Rocha, H.A.O.; Alves Junior, C. Effect of plasma-nitrided titanium surfaces on the differentiation of pre-osteoblastic cells. *Artif. Organs* **2019**, *43*, 764–772. [[CrossRef](#)] [[PubMed](#)]
32. Yang, F.; Huo, D.; Zhang, J.; Lin, T.; Zhang, J.; Tan, S.; Yang, L. Fabrication of graphene oxide/copper synergistic antibacterial coating for medical titanium substrate. *J. Colloid Interface Sci.* **2023**, *638*, 1–13. [[CrossRef](#)] [[PubMed](#)]
33. Alaoui, C.H.; Fatimi, A. A 20-year patent review and innovation trends on hydrogel-based coatings used for medical device biofabrication. *J. Biomater. Sci.-Polym. Ed.* **2023**, *34*, 1255–1273. [[CrossRef](#)]
34. Zia, A.W.; Anastopoulos, I.; Panayiotidis, M.I.; Birkett, M. Soft diamond-like carbon coatings with superior biocompatibility for medical applications. *Ceram. Int.* **2023**, *49*, 17203–17211. [[CrossRef](#)]
35. Bracic, M.; Potrc, S.; Finsgar, M.; Gradis, L.; Maver, U.; Budasheva, H.; Korte, D.; Franko, M.; Zemljic, L.F. Amoxicillin doped hyaluronic acid/fucoidan multifunctional coatings for medical grade stainless steel orthopedic implants. *Appl. Surf. Sci.* **2022**, *611*, 155621. [[CrossRef](#)]
36. Guan, J.; Jiang, X.; Xiang, Q.; Yang, F.; Liu, J. Corrosion and tribocorrosion behavior of titanium surfaces designed by electromagnetic induction nitriding for biomedical applications. *Surf. Coat. Technol.* **2021**, *409*, 126844. [[CrossRef](#)]
37. Kazemi, M.; Ahangarani, S.; Esmailian, M.; Shanaghi, A. Investigation on the corrosion behavior and biocompatibility of Ti-6Al-4V implant coated with HA/TiN dual layer for medical applications. *Surf. Coat. Technol.* **2020**, *397*, 126044. [[CrossRef](#)]
38. Shanaghi, A.; Souri, A.R.; Saedi, H.; Chu, P.K. Effects of the tantalum intermediate layer on the nanomechanical properties and biocompatibility of nanostructured tantalum/tantalum nitride bilayer coating deposited by magnetron sputtering on the nickel titanium alloy. *Appl. Nanosci.* **2021**, *11*, 1867–1880. [[CrossRef](#)]
39. Liu, Y.; Yang, Y.; Dong, D.; Wang, J.; Zhou, L. Improving wear resistance of Zr-2.5Nb alloy by formation of microtextured nitride layer produced via laser surface texturing/plasma nitriding technology. *Surf. Interfaces* **2020**, *20*, 100638. [[CrossRef](#)]
40. Braz, J.K.F.S.; Martins, G.M.; Sabino, V.; Vitoriano, J.O.; Barboza, C.A.G.; Soares, A.K.M.C.; Rocha, H.A.O.; Oliveira, M.F.; Alves Junior, C.; Moura, C.E.B. Plasma nitriding under low temperature improves the endothelial cell biocompatibility of 316L stainless steel. *Biotechnol. Lett.* **2019**, *41*, 503–510. [[CrossRef](#)]
41. Perez, E.; Pazos, L.; De las Heras, E.; Parodi, B.; Corengia, P.; Bracerias, I. Wear behaviour of UHMWPE against DC-Pulsed plasma nitrided and duplex treated AISI 316L used in hip joint replacements. *Plasma Process. Polym.* **2009**, *6*, S75–S80. [[CrossRef](#)]
42. Cubillos, G.I.; Romero, E.; Umana-Perez, A. ZrN-ZrO(x)Ny vs. -ZrO2-ZrOxNy coatings deposited via unbalanced DC magnetron sputtering. *Sci. Rep.* **2021**, *11*, 18926. [[CrossRef](#)]
43. Ul-Hamid, A. Synthesis microstructural characterization and nanoindentation of Zr, Zr-nitride and Zr-carbonitride coatings deposited using magnetron sputtering. *J. Adv. Res.* **2021**, *29*, 107–119. [[CrossRef](#)]
44. Yuan, S.; Lin, N.M.; Zeng, Q.F.; Zhang, H.X.; Liu, X.P.; Wang, Z.H.; Wu, Y.C. Recent developments in research of double glow plasma surface alloying technology: A brief review. *J. Mater. Res. Technol.* **2020**, *9*, 6859–6882. [[CrossRef](#)]
45. Grenadyorov, A.S.; Oskirko, V.O.; Zakharov, A.N.; Goncharenko, I.M.; Semenov, V.A.; Rabotkin, S.V.; Soloyev, A.A. Hydrogen-free active screen plasma nitriding of AISI 316L stainless steel. *Met. Mater. Int.* **2022**, *29*, 1498–1509. [[CrossRef](#)]
46. Qi, Y.; Liang, W.P.; Miao, Q.; Yi, J.W.; Lin, H.; Liu, Y.Y.; Ma, H.R. Role of the nitrogen ratio on mechanical properties and wear resistance of CrN/Fe functionally graded coating produced by double glow plasma alloying. *Appl. Surf. Sci.* **2022**, *585*, 152735. [[CrossRef](#)]
47. Sousa, F.A.; da Costa, J.A.P.; de Sousa, R.R.M.; Barbosa, J.C.P.; de Araujo, F.O. Internal coating of pipes using the cathodic cage plasma nitriding technique. *Surf. Interfaces* **2020**, *21*, 100691. [[CrossRef](#)]
48. Lou, J.; Ren, B.B.; Zhang, J.; He, H.; Gao, Z.L.; Xu, W. Evaluation of biocompatibility of 316L stainless steels coated with TiN, TiCN, and Ti-DLC films. *Coatings* **2022**, *12*, 1073. [[CrossRef](#)]
49. Smyrnova, K.; Sahul, M.; Harsani, M.; Pogrebnjak, A.; Ivashchenko, V.; Beresnev, V.; Stolbovoy, V.; Caplovic, L.; Caplovicova, M.; Vanco, L. Microstructure, mechanical and tribological properties of advanced layered WN/MeN (Me = Zr, Cr, Mo, Nb) nanocomposite coatings. *Nanomaterials* **2022**, *12*, 395. [[CrossRef](#)]

50. Hu, J.; Shi, Y.N.; Sauvage, X.; Sha, G.; Lu, K. Grain boundary stability governs hardening and softening in extremely fine nanograined metals. *Science* **2017**, *355*, 1292–1296. [[CrossRef](#)]
51. AlMotasem, A.T.; Daghbouj, N.; Sen, H.S.; Mirzaei, S.; Callisti, M.; Polcar, T. Influence of HCP/BCC interface orientation on the tribological behavior of Zr/Nb multilayer during nanoscratch: A combined experimental and atomistic study. *Acta Mater.* **2023**, *249*, 118832. [[CrossRef](#)]
52. Dong, W.; Yang, X.; Song, F.; Wu, M.; Zhu, Y.; Wang, Z. Anti-friction and wear resistance analysis of cemented carbide coatings. *Int. J. Adv. Manuf. Technol.* **2022**, *122*, 2795–2821. [[CrossRef](#)]
53. Zhai, W.; Bai, L.; Zhou, R.; Fan, X.; Kang, G.; Liu, Y.; Zhou, K. Recent progress on wear-resistant materials: Designs, properties, and applications. *Adv. Sci.* **2021**, *8*, 2003739. [[CrossRef](#)]
54. Mohamed, A.M.A.; Abdullah, A.M.; Younan, N.A. Corrosion behavior of superhydrophobic surfaces: A review. *ARAB J. Chem.* **2015**, *8*, 749–765. [[CrossRef](#)]
55. Amirnejad, M.; Rajabi, M.; Jamaati, R. The effect of crystallographic texture as a distinct effective parameter on the biocorrosion performance of Ti6Al4V alloy in PBS solution. *Corros. Sci.* **2021**, *179*, 109100. [[CrossRef](#)]
56. Datta, S.; Das, M.; Balla, V.K.; Bodhak, S.; Murugesan, V.K. Mechanical, wear, corrosion and biological properties of arc deposited titanium nitride coatings. *Surf. Coat. Technol.* **2018**, *344*, 214–222. [[CrossRef](#)]
57. Zhao, X.; Wang, B.; Lai, W.; Zhang, G.; Zeng, R.; Li, W.; Wang, X. Improved tribological properties, cyto-biocompatibility and anti-inflammatory ability of additive manufactured Ti-6Al-4V alloy through surface texturing and nitriding. *Surf. Coat. Technol.* **2021**, *425*, 127686. [[CrossRef](#)]

Disclaimer/Publisher’s Note: The statements, opinions and data contained in all publications are solely those of the individual author(s) and contributor(s) and not of MDPI and/or the editor(s). MDPI and/or the editor(s) disclaim responsibility for any injury to people or property resulting from any ideas, methods, instructions or products referred to in the content.